

## Forecasting of Chaotic Cloud Absorption Time Series for Meteorological and Plume Dispersion Modeling

V. PÉREZ-MUÑUZURI

*Group of Nonlinear Physics, Faculty of Physics, University of Santiago de Compostela, Santiago de Compostela, Spain*

(Manuscript received 18 June 1997, in final form 26 December 1997)

### ABSTRACT

A nonlinear forecasting method based on the reconstruction of a chaotic strange attractor from about 1.5 years of cloud absorption data obtained from half-hourly Meteosat infrared images was used to predict the behavior of the time series 24 h in advance. The forecast values are then used by a meteorological model for daily prediction of plume transport from the As Pontes 1400-MW power plant in northwestern Spain. Results from the meteorological model, using the cloud absorption predictions, are compared with measurements obtained from meteorological towers and a Remtech PA-3 sodar. The effects of cloud absorption on SO<sub>2</sub> ground-level concentration forecasts are analyzed for two different days.

### 1. Introduction

The accuracy of earth radiation budget estimates derived from satellite-based measurements is highly dependent on how well cloud variability is taken into account. Because of its dynamic nature and pronounced optical characteristics, cloud cover is one of the most important variables affecting the radiation balance, which, for example, is the determinant for dispersion modeling of pollutants and, ultimately, the global climate, among other effects. Different measurements and methods have been undertaken in the last decades (Vonder Haar et al. 1981; Minnis and Harrison 1984; Li et al. 1995) since the launch of the first weather satellite (Arking 1964). On the other hand, it is well known that diurnal and annual cycles of cloud cover occur in many areas (Short and Wallace 1980), but the magnitude and timing of these cloud oscillations and their radiative properties are poorly known.

In this work, an air pollution system for 24-h forecasting of mesoscale plume transport is presented. The system is based on a three-dimensional time-dependent meso- $\beta$  hydrostatic meteorological model and a Lagrangian adaptive plume model (Ludwig et al. 1989; Souto et al. 1994; Souto et al. 1998). These models are already being used, on a trial basis, at the As Pontes power plant in the northwest of Spain. Because the whole system was designed for running daily on a medium-sized workstation, the meteorological prediction

model has been developed for providing good mesoscale meteorological forecasting with little CPU cost.

The area under consideration is characterized by steep hills and sea inlets bathed by the Atlantic Ocean surrounded by cliffs, consequently affecting the wind direction. Figure 1 shows the topography of the area (61 km  $\times$  61 km) whose central point is the As Pontes power plant (here a continuous gaseous plume is exhausted at 356.5 m above ground level, 688.4 m above the sea level). This area is between between 43°9' and 43°40' N and 7°36' and 8°12' W. The top of the region is the Serra do Xistral, 1036 m above sea level. Thus, the region under consideration can be considered as an intermediate terrain. The region is mainly influenced by northeastern and southwestern winds that displace the power plant plume from and to the region of interest. To predict its behavior, the meteorological model should account for cloud behavior and formation, which means to describe a larger region to take into account the displacement of clouds. So, to avoid longer extensive calculations usually beyond the capabilities of an industry, a forecasting model for cloud formation was developed based on nonlinear chaotic predictions that are coupled to the meteorological model describing wind and temperature behaviors.

Here, we have tried to combine two different points of view of analyzing meteorological data, namely, the standard atmospheric circulation models and a new approach based on the analysis of time series data of physical observations, whose dynamics exhibit irregular or chaotic behavior. In the former case, physical information about weather and climate dynamics is obtained by studying the "bulk" properties (averages, covariances, etc.) of basic meteorological field variables. The

---

*Corresponding author address:* Dr. Vicente Pérez-Muñuzuri, Group of Nonlinear Physics, Faculty of Physics, University of Santiago de Compostela, 15706 Santiago de Compostela, Spain.  
E-mail: vicente@fmmeteo.usc.es

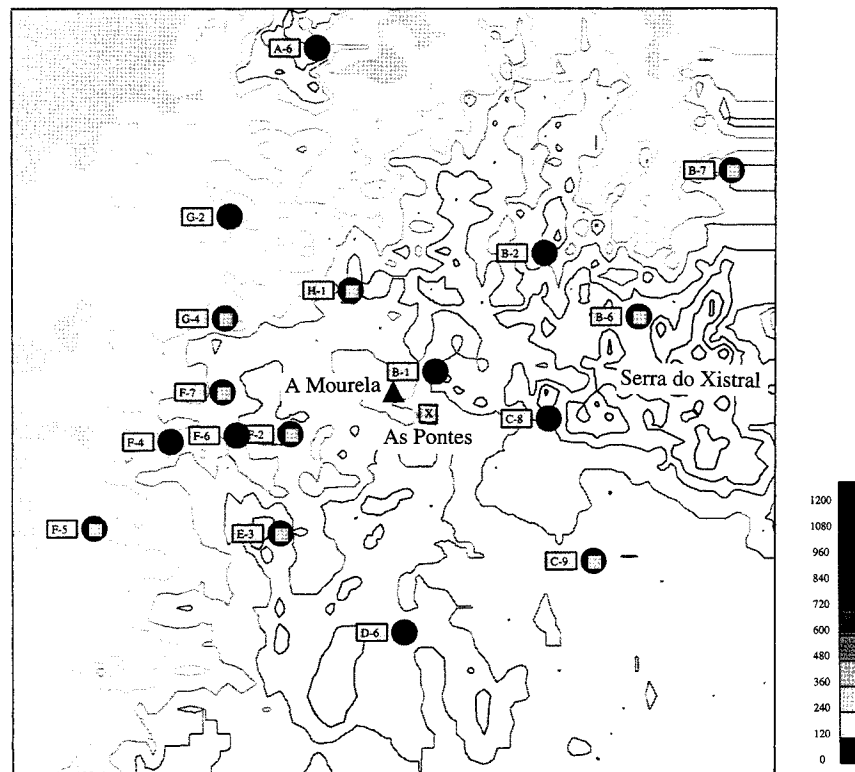


FIG. 1. Topography of the area under study in northwestern Spain (Galicia). Oceanic areas (gray zones) can be observed in the north and west of the figure. Meteorological towers are indicated as squares, circles indicate the position of GLC stations, and the sodar (black triangle) is located at the center of the figure in A Mourela. The As Pontes 1400-MW power plant is shown by an "X."

latter case, which may be called *nonlinear time series analysis*, explores the possibility and the extent to which the dynamics generating this time series is deterministic, that is, occurs on a low-dimensional, chaotic attractor. This analysis has already been applied to a variety of large-scale physical problems, from Rayleigh-Bénard convection (Malraison et al. 1983) to geostrophic turbulence (Guckenheimer and Buzyna 1983); from surface temperature (Bountis et al. 1993) to earthquake dynamics (Pavlos et al. 1994); and from surface gravity waves (Elgar and Mayer-Kress 1989) to weather and climate dynamics (Fraedrich 1986; Nicolis and Nicolis 1984). In many cases, evidence of a low-dimensional chaotic attractor has been observed, even if the time series is not free of noise.

Here, we apply the techniques of nonlinear analysis to a time series of semihourly cloud absorption values obtained from infrared Meteosat images for 24-h forecasting. Later, the cloud absorption values are introduced in a meteorological model for wind and temperature forecasting in the region of interest and compared with measurements from nine meteorological towers and one Remtech PA-3 sodar. The role of cloud absorption determining ground-level  $\text{SO}_2$  concentrations

is analyzed for two different days in the summer and winter of 1996.

## 2. Meteorological model

The dynamics of the atmospheric boundary layer depends on complex interactions of various influences: local topography, vegetation, clouds, radiation and moisture flux, and other processes. During the last two decades, many three-dimensional models have been formulated to describe special mesoscale phenomena (Yamada and Mellor 1975; Pielke 1984; Enger 1990; Warner and Seaman 1990; Enger et al. 1993; Stauffer et al. 1993; Weygandt and Seaman 1994).

### a. Equations

The present dynamic model is a three-dimensional time-dependent mesoscale model based on finite difference solutions of the hydrothermodynamic equations. Only the hydrostatic part has been solved here (Souto et al. 1994; Souto et al. 1996; Souto et al. 1998; Pérez-Muñozuri et al. 1996). A terrain-following coordinate system is used to introduce the topography in the model

(Pielke and Martin 1981). The new vertical coordinate  $\eta$  is defined as

$$\eta = s \frac{z - z_g}{s - z_g}, \quad (1)$$

where  $z_g$  is the terrain height. The maximum height  $s$  is taken constant in this study and equal to 7000 m. The basic equations of the model for the horizontal wind components  $U$ ,  $V$ ; the potential temperature  $\theta$ ; and the specific humidity  $q_3$  can be written as

$$\begin{aligned} \frac{DU}{Dt} = & \left( \frac{s}{s - z_g} \right)^2 \frac{\partial}{\partial \eta} \left( K_m \frac{\partial U}{\partial \eta} \right) - \overline{u \frac{\partial u}{\partial x}} - \overline{v \frac{\partial u}{\partial y}} - \theta \frac{\partial \pi}{\partial x} \\ & + g \left( \frac{\eta - s}{s} \right) \frac{\partial z_g}{\partial x} - \hat{f}W + fV, \end{aligned} \quad (2)$$

$$\begin{aligned} \frac{DV}{Dt} = & \left( \frac{s}{s - z_g} \right)^2 \frac{\partial}{\partial \eta} \left( K_m \frac{\partial V}{\partial \eta} \right) - \overline{u \frac{\partial v}{\partial x}} - \overline{v \frac{\partial v}{\partial y}} - \theta \frac{\partial \pi}{\partial y} \\ & + g \left( \frac{\eta - s}{s} \right) \frac{\partial z_g}{\partial y} - fU, \end{aligned} \quad (3)$$

$$\frac{D\theta}{Dt} = \left( \frac{s}{s - z_g} \right)^2 \frac{\partial}{\partial \eta} \left( K_h \frac{\partial \theta}{\partial \eta} \right) - \overline{u \frac{\partial \theta}{\partial x}} - \overline{v \frac{\partial \theta}{\partial y}} + S_\theta, \quad (4)$$

and

$$\frac{Dq_3}{Dt} = \left( \frac{s}{s - z_g} \right)^2 \frac{\partial}{\partial \eta} \left( K_q \frac{\partial q_3}{\partial \eta} \right) - \overline{u \frac{\partial q_3}{\partial x}} - \overline{v \frac{\partial q_3}{\partial y}}, \quad (5)$$

where  $f$  and  $\hat{f}$  denote the Coriolis parameters [ $f = 1.45 \times 10^{-4} \sin(\phi)s^{-1}$ ,  $\hat{f} = 1.45 \times 10^{-4} \cos(\phi)s^{-1}$ , and  $\phi$  is the latitude at the area under consideration, which in general will be a function of the position  $x$ ,  $\phi(x)$ ]. Finally, to complete the calculations of the wind field, the vertical component of the wind velocity  $W$  is obtained from the conservation of mass relationship.

The horizontal subgrid correlation terms in Eqs. (2)–(5) (denoted by an upper bar) are supposed to be small compared to the advection terms, and so some authors exclude them from the calculations (Enger 1990). Occasionally, these fluxes have been used as free parameters to minimize the discrepancies between the numerical method and the experimental data (Pérez-Muñuzuri et al. 1995) or to control nonlinear aliasing by choosing a parameterization depending on the horizontal wind gradients modulated by some coefficient  $k_D$ , arbitrarily adjusted until  $2\Delta_x$  wavelengths do not appear to degrade the solutions significantly (Pielke 1984). Here, Tag et al.'s (1979) parameterization for the eddy formulation with  $k_D = 0.2$  is followed.

The vertical turbulent fluxes correspond to those terms with the exchange coefficients for momentum, heat, and moisture,  $K_m$ ,  $K_h$ , and  $K_q$  in Eqs. (2)–(5). They account for the vertical mixing at the atmosphere, and their definitions depend on the stability of the layer being simulated. When the layer is stably stratified (such

as at night over land or on cloudy days with wet ground), we use a parameterization based on the Richardson number suggested by Blackadar (1979). On the other hand, when the atmospheric layer is unstably or neutrally stratified (such as over land or sunny days) the exchange coefficients are then defined as a function of the distance above the ground, and O'Brien's (1970) cubic polynomial approximation is used. To apply this profile formulation, the depth of the planetary boundary layer (PBL) must be known.

The depth of the planetary boundary layer  $z_i$  is usually associated with an inversion, and it is calculated, during the daytime, as suggested by Deardorff (1974) and Pielke and Mahrer (1975), using a prognostic equation that mainly depends on the surface heating (Pielke 1984). With the use of the slab model, which considers the entrainment layer infinitesimal, Deardorff has derived the following equation for the growth of the convective PBL, which includes the effects of the entrainment:

$$\begin{aligned} \frac{\partial z_i}{\partial t} = & -U_{z_i} \frac{\partial z_i}{\partial x} - V_{z_i} \frac{\partial z_i}{\partial y} + W_{z_i} \\ & + \frac{1.80w_*^3 + 1.98u_*^3 - 5.94u_*^2 f z_i}{g\psi \frac{z_i^2}{\theta_s} + 9w_*^2 + 7.2u_*^2}, \end{aligned} \quad (6)$$

where

$$w_* = \begin{cases} \left( -\frac{g}{\theta_s} u_* \theta_* z_i \right)^{1/3}, & \text{if } \theta_* \leq 0 \\ 0 & \text{if } \theta_* > 0, \end{cases} \quad (7)$$

and  $\theta_s$  is the potential temperature at the top of the surface layer,  $h_s = 0.04z_i$ . In Eq. (6) the growth of  $z_i$  is directly proportional to the surface heat flux and mesoscale vertical velocity and inversely proportional to the overlying stability.

During the transition from convective to stable conditions,  $z_i$  tends to adjust exponentially toward an equilibrium depth (Konratyev 1969), with a response time of  $1/f$ . The expression of Smeda (1979), who proposed that the growth of the stable layer is proportional to the stress induced by the wind near the surface has been used,

$$z_i^{\text{eq}} = \frac{0.3u_*}{f}. \quad (8)$$

The height calculated by Eq. (8) during transition time could be considered as a fictitious height during which the stable layer near the surface develops and becomes well established, so the model provides a value for the PBL throughout the simulation period.

The similarity stability functions given by Businger et al. (1971) are used to account for the turbulence parameters needed to solve these equations. Here,  $q_*$ ,  $\theta_*$ , and  $u_*$  are obtained by applying the two-level method proposed by Berkowicz and Prahm (1982). It consists

of an iterative process that converges quickly. It uses wind speed and potential temperature at two different heights (in this case, 3 and 10 m) as inputs. For the model presented here, this two-level method works better than that using a least squares approach described by San José (1991), which requires more accurate results at the surface layer.

### b. Numerical method

Equations (2)–(5) are solved by a finite difference method. A forward-in-time, upstream-in-space scheme is used for the advection terms. For the diffusion terms (vertical turbulent fluxes), a semi-implicit scheme with weight of 75% on a future time step is used and the constant time step is 30 s. The rest of spatial derivatives are solved by a forward-in-time, centered-in-space scheme. For Coriolis terms, as well as for the radiation terms, an explicit scheme has been used.

By using an upwind scheme for the advection terms, nonlinear waves appear, disturbing the solution. Although an eddy parameterization of the horizontal turbulent fluxes has been used to minimize these effects, two-dimensional filtering based on the averaging of  $U$ ,  $V$ ,  $W$ ,  $\theta$ , and  $q_3$  with the nearest neighbors with some factor  $\alpha$  (see Haltiner and Williams 1980) has also been required.

Forty logarithmically spaced vertical levels between 3 m above the ground and the domain top at  $s = 7000$  m are used. A  $31 \times 31$  horizontal grid with a grid mesh of 2000 m is used.

Both the continuity and hydrostatic pressure equations are integrated by an explicit finite-difference scheme in order to obtain the vertical component  $W$  of the wind velocity and the scaled pressure  $\pi$ .

### c. Initial and boundary conditions

Twenty-four-hour meso- $\alpha$  forecasts are provided daily by the Spanish National Meteorological Institute for four points on a 100-km grid at four pressure levels. The forecasts are used as initial data in our meteorological model, which provides meso- $\beta$  forecasts of three-dimensional wind, potential temperature, and specific humidity fields. To avoid the first spurious effects from initialization, the model is run for 1 h without time-dependent forcing terms.

Lateral boundary conditions for the spatial derivatives at each level are inflow and gradient outflow for the horizontal wind components and zero-flux boundary conditions for pressure  $\pi$ , potential temperature, and specific humidity. Surface temperature and specific humidity are initialized from measurements obtained from nine meteorological towers in the area of interest. An initial constant profile for  $q_3$  is supposed until reaching the PBL and from there on  $q_3$  linearly decreases to zero. The depth of the planetary boundary layer  $z_i$  initially,

at night, is supposed to be very small and here was set to 100 m.

In the terrain-following coordinate system,  $z_g$  is defined as the sum of the terrain height, the zero displacement, and the surface roughness length. Then, by definition, the wind at  $\eta = 0$  is zero. The derivatives of the horizontal wind components at the upper boundary are set to zero (i.e., homogeneous geostrophic wind). The vertical gradient of potential temperature and specific humidity at the model top are assumed constant. The temperature at the ground is calculated by means of a force–restore method described in the next section, while specific humidity at the ground surface is calculated by a method proposed by McCumber and Pielke (1991), which mainly depends on the surface temperature.

### d. Surface temperature

#### 1) EARTH–ATMOSPHERE HEAT BUDGET

The following equation, termed the force–restore method by Deardorff (1978), was used to predict the air–earth interface temperature  $T_G$ :

$$\frac{\partial T_G}{\partial t} = \frac{1}{\rho_s c_s} \left( \frac{4\pi}{k_s Y} \right)^{1/2} [(1 - \alpha_s) Q_S + Q_{LD} - Q_{LU} - Q_H - Q_E] - \frac{2\pi(T_G - T_M)}{Y}. \quad (9)$$

The last term in Eq. (9) includes the effect of conduction from the ground below the interface. It avoids the problem of having to compute temperatures at a number of levels beneath the surface. Here,  $T_M$  is calculated as

$$\frac{\partial T_M}{\partial t} = \frac{1}{Y} (T_G - T_M). \quad (10)$$

The soil properties  $\alpha_s$ ,  $\rho_s$ ,  $c_s$ , and  $k_s$  depend on the surface nature and sun position. Most typical values can be found in the literature; five different soil types were used for our simulations (Souto 1998).

The heat flux values  $Q_S$ ,  $Q_{LD}$ ,  $Q_{LU}$ ,  $Q_H$ , and  $Q_E$  change with solar elevation and have been calculated following parameterizations described in Pielke (1984) and Stull (1991). The solar radiative flux  $Q_S$  is computed from the equation

$$Q_S = [1 - \xi(t)](S - A_s) \cos Z, \quad (11)$$

where  $\xi$  is the sum of the cloud-top albedo and in-cloud absorption by cloud droplets;  $\xi$  can change with time. Clouds are assumed to be in one layer at a height that is the average height weighted by the amount of each layer observed from the surface. Typical values of  $\xi$  from the literature are shown in Table 1.

The downward and upward longwave radiation flux

TABLE 1. Typical values of cloud absorption.

Cloud type	$\xi$
High cloud	0.20
Middle cloud	0.56
Low cloud other than cumulonimbus	0.59
Cumulonimbus	0.95

are calculated from a formulation given by Idso and Jackson (1969)<sup>1</sup>:

$$Q_{LD} - Q_{LU} = \sigma(\{F\downarrow[1 - \xi(t)] + \xi(t)\}T_a^4 - T_G^4), \quad (12)$$

where the downward longwave irradiance  $F\downarrow$  is given by

$$F\downarrow = 1 - 0.261 \exp[-7.77 \times 10^{-4} (273.15 - T_a)^2], \quad (13)$$

and  $T_a$  is determined at Stevensen screen height (1.5 m).

Finally,  $Q_H$  and  $Q_E$  are calculated as

$$Q_H + Q_E = -\bar{\rho}u_*(C_p\theta_* + L_vq_*). \quad (14)$$

## 2) OCEAN-ATMOSPHERE HEAT BUDGET

A formulation given by Portela and Neves (1994) is used to compute heat exchanges across the water surface, neglecting the bottom heat flux and other minor sources and sinks. Similar formulations have been the subject of several papers in the literature (e.g., Orlob and Marjanovic 1989; Blanke and Delecluse 1993). The heat fluxes in this formulation also depend on the cloud absorption parameter  $\xi$ .

The time rate of change of water surface temperature  $T_w$  is determined by

$$\frac{\partial T_w}{\partial t} = \frac{1}{\rho_w c_w H} (Q_S + Q_A + Q_W + Q_E + Q_H), \quad (15)$$

where heat fluxes are given by the following set of equations:

$$Q_S = S A_s [1 - 0.65\xi^2(t)](1 - \alpha_w) \cos Z, \quad (16)$$

where the albedo of the water surface  $\alpha_w$  is supposed to depend on the solar elevation as  $\alpha_w = -0.0139 + 0.0467 \tan Z$ .

$$Q_A = 0.909 \times 10^{-5} \sigma [1 + 0.17\xi^2(t)] T_a^6, \quad (17)$$

$$Q_W = -0.97 \sigma T_w^4, \quad (18)$$

and

$$Q_E = \begin{cases} -(a + b\bar{V}_1)(e_{sw} - e_{sa}R_h), & \text{if } (e_{sw} - e_{sa}R_h) > 0 \\ 0 & \text{if } (e_{sw} - e_{sa}R_h) \leq 0, \end{cases} \quad (19)$$

<sup>1</sup> See also Prata (1996) for a review of several other parameterizations.

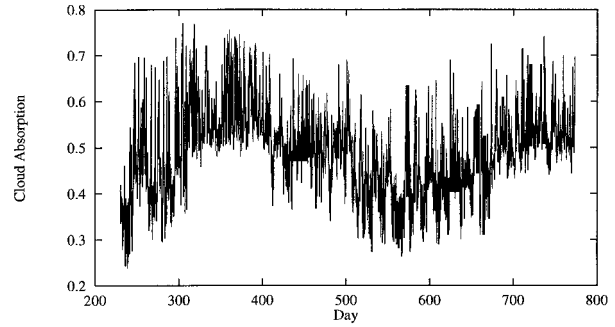


FIG. 2. Cloud absorption  $\xi$  series of semihourly measurements in northwestern Spain (Galicia) obtained from the Meteosat and consisting of 25 000 points of data (approximately 1.5 years). The time series begins on August 1995, where day 1 is 1 Jan 1995.

where  $\bar{V}_1$  is the wind speed calculated in the first level over the sea surface,  $a = 0.075 \text{ W m}^{-2} \text{ Pa}^{-1}$  and  $b = 0.03 \text{ J m}^{-3} \text{ Pa}^{-1}$  are constants of the wind function, and  $e_{sw}$  and  $e_{sa}$  are the saturation vapor pressure at the water temperature and at the air temperature (Pa), respectively. The saturation pressure is given by

$$e_s = 612 \exp\left(\frac{17.5t}{241 + t}\right), \quad (20)$$

where  $t$  is the temperature ( $^{\circ}\text{C}$ ). Finally the sensible heat flux  $Q_H$  is calculated as

$$Q_H = -\gamma(a + b\bar{V}_1)(T_w - T_a). \quad (21)$$

## e. Nonlinear prediction

Equations (1)–(21) are used to forecast the meteorological conditions 24 h in advance and a continuous set of values of  $\xi$  must be provided in order to close the model. We have collected a time series of values of  $\xi$  during a year and a half from semihourly Meteosat infrared images of the region of interest in order to predict  $\xi$  (Fig. 2). We obtain a single average value of the cloud cover over the area of interest (northwestern Spain) from these images. Values range from 0 to 1, where  $\xi = 1$  means that no radiation is emitted at the surface. For clear skies, the stored value is close to zero; intermediate values depend on cloud thickness and water phase and content. Values of  $\xi(t)$  could also be considered to depend on  $x$  and  $y$ , but this would require higher-precision satellite images than are available from Meteosat. Furthermore, the noise in the time series increases with a finer image resolution, which decreases the precision of the nonlinear forecasting method depicted below.

In the following, the cloud dynamics are supposed to belong to the category of dissipative system dynamics, which can reveal dynamics with strange attractor structure. The Lyapunov exponents determine how far into the future one can make a successful forecast, and the number of variables needed to make the prediction is

governed by the fractal dimension (Grassberger and Procaccia 1983; Wolf et al. 1985). The general nonlinear prediction method reconstructs the strange attractor from the set of data in a minimum embedding space dictated by the correlation fractal dimension and then predicts the future using a local forecasting function computed from the attractor (Farmer and Siderowich 1987; Casdagli 1989; Sugihara and May 1990; Abarbanel et al. 1990; Abarbanel et al. 1993; Abarbanel 1996). Takens (1981) has proven that, after embedding, and if the embedding dimension  $m$  and time delay  $\tau$  are chosen appropriately, there exists a smooth map  $\mathcal{F}$  such that

$$\xi_{n+T} = \mathcal{F}(\Xi_n), \tag{22}$$

where  $\Xi_n$  is a vector of data points defined by

$$\Xi_n = [\xi_n, \xi_{n+\tau}, \dots, \xi_{n+(m-1)\tau}], \tag{23}$$

$n$  is the number of data points in the time series, and  $T$  is the forecasting time.

The meaning of the theorem is that, under some general conditions, the orbit followed by  $\Xi_n$  in this  $m$ -dimensional embedding space will differ from the actual solution of  $\mathcal{F}(\Xi_n)$  in Eq. (22) only by a smooth change of coordinates. The most common solution of Eq. (22) is to compute the Jacobian of the strange attractor in the vicinity of a target point and then use it to predict the future of that point. Typically one finds two to five times the minimum number of nearest neighbors  $k$  needed to compute the Jacobian and makes a least squares fit using the nearest neighbors and their future iterates to compute the prediction function  $\mathcal{F}$ . This must be repeated for every target point. The procedure consists of the following steps.

- Choose an embedding dimension  $m$ , an embedding delay  $\tau$ , and a forecasting time  $T$  (see appendix A).
- Choose a vector  $\Xi_i$  by using Eq. (23).
- Find the  $k$  nearest neighbors  $\Xi_j$  of  $\Xi_i$  using the Euclidean distance.
- Order the neighbors from closest to farthest and find an affine model of the following form:

$$\xi_{j(l)+T} \approx \alpha_0 + \sum_{n=1}^m \alpha_n \xi_{j(l)-(n-1)\tau}, \quad l = 1, \dots, k, \tag{24}$$

where  $\xi_{j(l)}$  is the  $j$ th coordinate of the  $l$ th neighbor of  $\Xi_i$ , and the  $\alpha_0, \dots, \alpha_m$  are the parameters of the model, computed by ordinary least squares.

To evaluate the accuracy of the nonlinear predictions, the normalized root-mean-square error (rmse) (Farmer and Siderowich 1987) is used:

$$E = \left\{ \frac{\sum_i [\xi_{\text{pred}}(i) - \xi(i)]^2}{\sum_i [\xi(i) - \bar{\xi}]^2} \right\}^{1/2}, \tag{25}$$

where  $\xi_{\text{pred}}(i)$  is the predicted value of the measured  $\xi(i)$

24 h later and  $\bar{\xi}$  is the mean of the time series during the forecasting period of time. If  $E = 0$ , the predictions are perfect;  $E = 1$  indicates that the performance is no better than a constant predictor  $\xi_{\text{pred}}(i) = \bar{\xi}$ .

### 3. Results

In the following, we apply the chaotic analysis described in the previous section and appendix A to the cloud absorption data to achieve 1) an estimation of the correlation dimension for determining the embedding dimension  $m$ , 2) an estimation of the largest Lyapunov exponent, and 3) the forecasting of cloud absorption from Eq. (24) for different days.

Later, using the predicted values of cloud absorption, the hydrostatic meteorological model is run, and the obtained results are compared with real meteorological data obtained from nine meteorological towers and a one Remtech PA-3 sodar located in the area of simulation. Finally, the sensitivity of the model to the cloud absorption parameter is analyzed in terms of the ability of the meteorological model for plume dispersion forecasting.

#### a. Chaotic analysis of the experimental time series

Stationarity is a necessary condition when the time series corresponds to the dynamic evolution of a strange attractor. Therefore, testing for stationarity should necessarily be the first step in any data analysis. Unfortunately, although a precise asymptotic definition of stationarity exists, there is no clear and unambiguous method for applying that definition in real finite time series. When applying nonlinear methods to time series, the problem becomes even more complicated since from a practical point of view, one must now be concerned explicitly with time variation of more subtle, nonlinear properties of the series (Manuca and Savit 1996). There is a significant body of literature on nonstationary tests (see, for some recent examples, Isliker and Kurths 1993 and Theiler and Eubank 1993) that often deals with the division of the time series into several windows where a common statistical property is measured and compared among the different divided parts of the series. Here, we test the stationarity of our series by plotting in Fig. 3 the probability density function of the first 20 000 and the full set of 25 000 points. Note that there is no significant time variations in that quantity. On the other hand, at least 1 year of data points should be taken for the test in order to guarantee the stationarity of the cloud absorption time series under investigation.

The chaotic character of the time series is revealed by the broadband form of the power spectrum (Fig. 4). Our results suggest that the time evolution of our data is governed by a strong deterministic component. Although the high-frequency part of the spectrum is dominated by the daily frequency  $w_1 = 1/24 \text{ h}^{-1}$ , it is also possible to observe a continuous band of frequencies

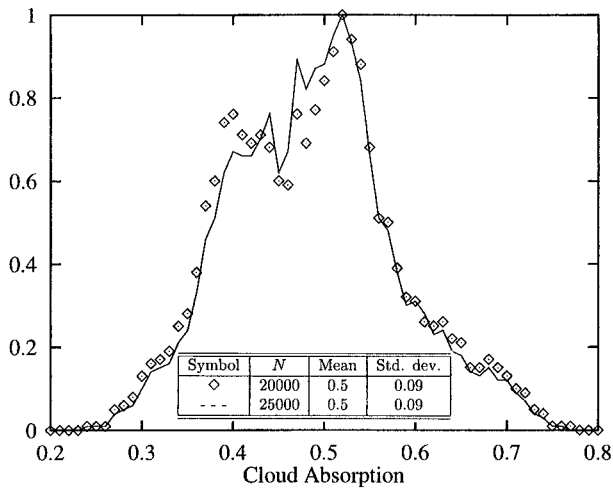


FIG. 3. Evidence of stationarity of the full time series.

that departs from the low-frequency part of the spectrum; this is where the annual frequency ( $\omega_0 = 1/8760 \text{ h}^{-1}$ ) of our data lies, which forms the large “sine-wave” variation observed in Fig. 2. So, the intermediate range of frequencies fits to the form  $P(\omega) \propto 1/\omega^\alpha$ , with  $\alpha \approx 1.6$ , which could lead to the conclusion that our data contains a strong colored noise component (Osborne and Provenzale 1989). This is also corroborated by the fact that the autocorrelation coefficient  $A(\tau)$  of our series; that is,

$$A(\tau) = \frac{1}{N} \sum_{i=1}^N (\bar{\xi}_i \times \bar{\xi}_{i+\tau})$$

and

$$\bar{\xi}_i = \xi_i - \frac{1}{N} \sum_{i=1}^N \xi_i, \quad (26)$$

does not decay very rapidly (Fig. 5), which also supports the idea that our data contains a noise component (Bountis et al. 1993).

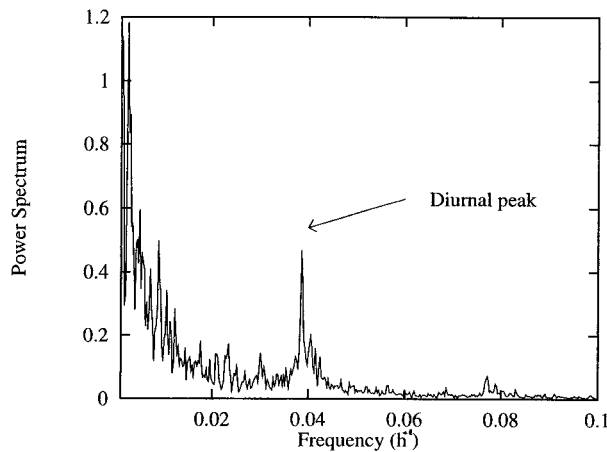


FIG. 4. Power spectrum of the full series.

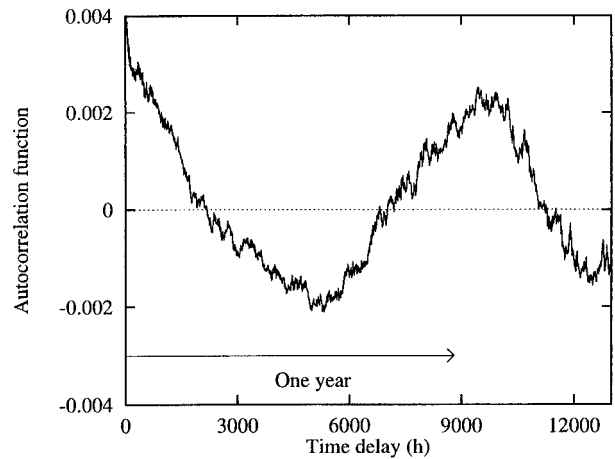


FIG. 5. The autocorrelation coefficient for the full series, showing evidence of “recurrence” after 1 year.

Figure 6 presents the estimated correlation integral  $C(r; m)$  for  $m$  up to 15 with clear scaling  $C(r; m) \approx r^{\nu(m)}$  for low values of distance  $r$  in phase space. The slope  $\nu(m)$  saturates as  $m$  increases at the value  $\nu = 5.4$ . This result was found to be invariable for time delay  $\tau = 25\text{--}350 \text{ h}$ . For larger time delays, a *knee* behavior appears in the plot of correlation integrals, which makes it difficult to calculate a proper correlation dimension  $\nu$ . If we compare the obtained value of the correlation dimension  $\nu$  with the value one expects from fractal (colored) noise (Osborne and Provenzale 1989),  $\nu_{\text{FN}} = 2/(\alpha - 1)$ , with  $\alpha = 1.6$ ,  $\nu_{\text{FN}} = 3.3$ , which is not close enough to the measured value of  $\nu = 5.4$  for one to

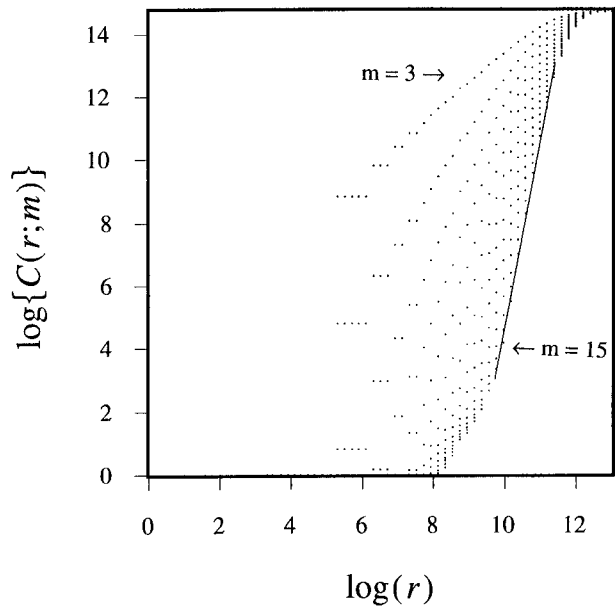


FIG. 6. Correlation function [Eq. (27)] vs distance  $r$  for different embedding dimensions  $m$  and time delay  $\tau = 25 \text{ h}$  for the full time series.

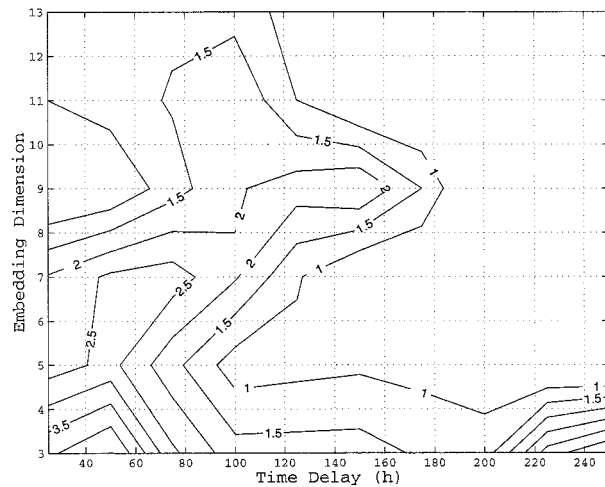


FIG. 7. Dependence of the largest Lyapunov exponent  $\lambda_{\max}$  on the embedding dimension  $m$  and time delay  $\tau$  [ $N = 20\,000$ , evolution step = 10, SCALMX = 10, SCALMN = 0, see (Wolf et al. 1985) for details].

claim that the full time series is dominated by colored noise. On the other hand, according to the embedding theory, the saturation value of the slope in the scaling region, as  $m$  increases, supports the existence of a low-dimensional attractor<sup>2</sup> with fractal dimension  $D = 5.4$ . Thus, the minimum time series length ( $N_{\min}$ ) calculated from Eq. (30) (see appendix A) is satisfied as the total length of the time series, which we have used for the results presented here, is  $N = 25\,000$ .

The chaotic (sensitive to initial conditions) character of the dynamic flow in the attractor is demonstrated by Fig. 7, which shows the estimation of the largest Lyapunov exponent  $\lambda_{\max}$  as a function of the embedding dimension  $m$  and the time delay  $\tau$ . When the dimensionality of the embedding space is reduced,  $\lambda_{\max}$  is expected to increase for a deterministic system because the attractor occupies a larger portion of the available space (Abarbanel et al. 1990; Abarbanel et al. 1993; Abarbanel 1996). Indeed, reducing the embedding space dimensions to three leads, in our case, leads to a significant increase in the Lyapunov exponent for any value of the time delay. Note that this behavior of  $\lambda_{\max}$  is quite distinct from what is observed for a random signal (Bountis et al. 1993). On the other hand, when  $\tau$  and  $m$  increase, the attractor tends to occupy a small portion of the available space, which gives rise to very small Lyapunov exponents (around zero) that do not appear in the contour plot. Then, the greatest positive values of  $\lambda_{\max}$  with physical meaning are found for middle values of  $m$  and values of  $\tau$  from about 40 to 80 h.

<sup>2</sup> It is interesting to note that the correlation dimension of the time-differenced series does not vary significantly from that of the original series, which confirms the deterministic nature of our data, even though it contains a small noise component (Bountis et al. 1993).

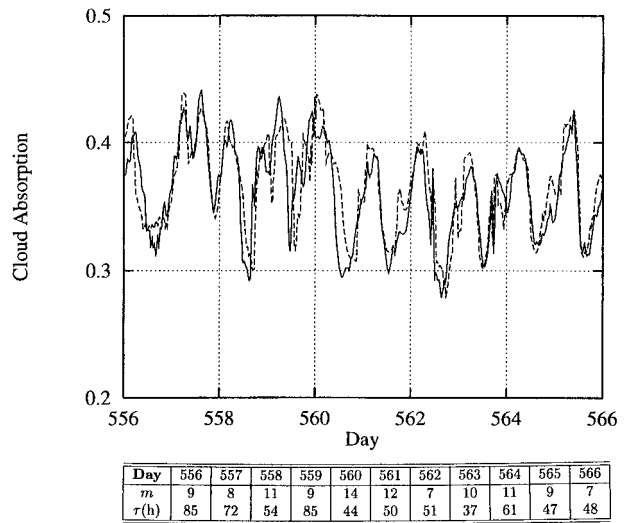


FIG. 8. Forecast values of the cloud absorption  $\xi$  (dashed line) from 10 to 20 July 1996 (days 556–566) compared with the measured values obtained from infrared images provided by the Meteosat (continuous line). The used values of the embedding dimension  $m$  and time delay  $\tau$  are shown in the table below the figure for each day.

The analysis of the cloud absorption time series showed the chaotic characteristics of our data, so we were able to construct a predictor map for our series using the method described in section 2e. This method forecasts the daily amount of cloud absorption 24 h in advance at the As Pontes power plant from the time series shown in Fig. 2. Then the resulting forecast is used as an input to the meteorological model that is used to calculate the wind and temperature fields in the area of interest. Here, in this study, we have selected 11 days, from 10 to 20 July 1996, for research purposes. During these days, middle clouds and strong temperatures occurred in northwestern Spain. Figure 8 shows the predicted values of  $\xi$  compared with the measured values obtained from the Meteosat, and the values of  $m$  and  $\tau$  used for the forecasting are shown in the table below the graph. Observe that those values agree with the arguments derived above for obtaining the maximum Lyapunov exponent. Most of the large oscillations in the time series were reproduced by our nonlinear forecasting method. For the 11 days selected for this study, the rmse of the cloud absorption forecasting [Eq. (25)] was lower than 25%.

*b. Meteorological results*

Cloud absorption forecasts were used as inputs to the hydrostatic meteorological model described earlier to obtain wind, potential temperature, and specific humidity fields for the area shown in Fig. 1.

Figure 9 shows the predicted and observed 10-m height wind speed, wind direction, and surface temperature measured at a meteorological station located at the As Pontes power plant (center of the grid) for 14 July,

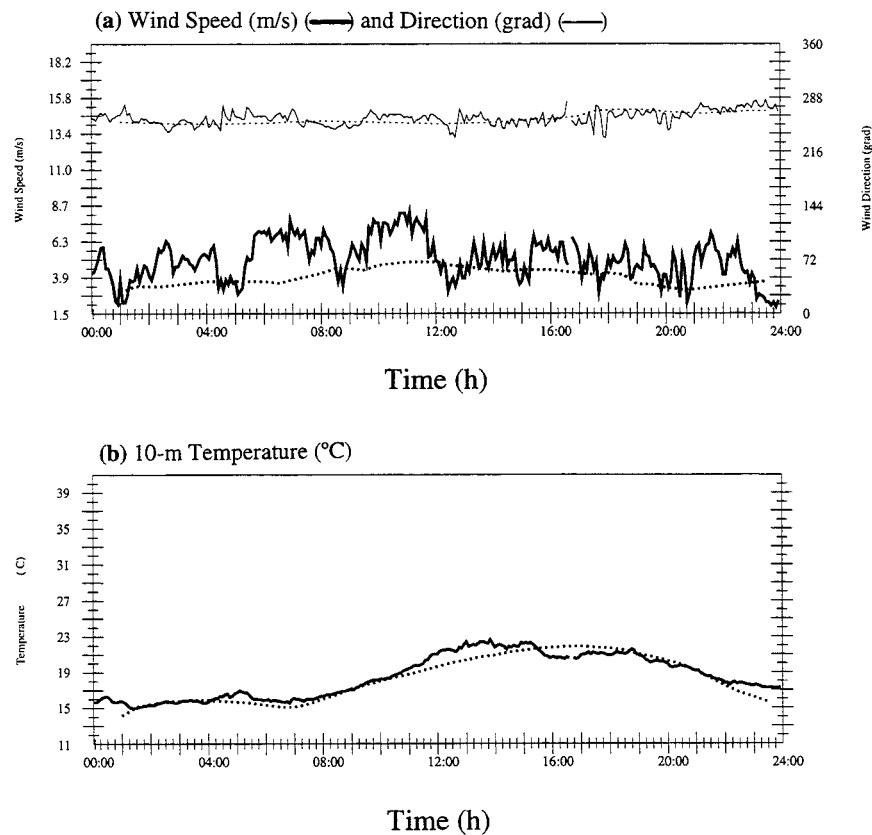


FIG. 9. Predicted (dots) and measured (line) wind speed, wind direction, and 10-m surface temperature at A Mourela (center of the grid) for 14 July 1996.

and Fig. 10 shows the results for 14 December 1996. The measurements are obtained at the meteorological towers every 5 min, while the model provides half-hourly averaged data that could explain some of the differences observed, especially those between the measured and predicted values of the wind speed. So although the forecasts for 14 July were correct both for temperature and wind fields, for 14 December, both wind speed and temperature approached the correct values during the forecast period, while the predicted wind direction maintained a constant difference from that measured at the meteorological station.

Measured temperature profiles provided by sodar were in agreement to the numerical predictions for both days (Figs. 11a,b). Note that the model reproduces the variations of temperature with height both under stable and convective situations and is in good agreement with the experimental data. In particular, the profile for 14 December (Fig. 11b) shows the development of the mixed layer below about 600 m, which was measured by the sodar around 1200 LST. This effect was probably due to cloud cover, which averaged about 70% that day.

Finally, surface temperatures predicted by the meteorological model for the 11 selected days (using the previously calculated cloud absorption values) are compared with observed values in Fig. 12 for two different

hours: night (0400 LST) and day (1400 LST). The measurements are from A Mourela, F-7, and E-3 meteorological stations (see Fig. 1). Figure 12 shows a good agreement between numerics and measurements.

### c. Plume dispersion forecasting

The importance of cloud absorption in meteorological modeling was highlighted for  $\text{SO}_2$  ground-level concentration (GLC) forecasting. Thus, in the following the predicted values of  $\xi(t)$  are modified in order to test the importance of this parameter for plume dispersion forecasting. Calculations were performed after modifying the predicted values of  $\xi(t)$  in Eqs. (11)–(21) and releasing 20 000 Lagrangian particles<sup>3</sup> from the 350-m stack at the As Pontes power plant at a rate of 20 particles per iteration. Figure 13 shows the vertical plume profile simulated for 1700 LST 14 July 1996. The particle model predicts the plume impact on the ground, which on that day was especially important about 20 km from the chimney.

<sup>3</sup> Here, we have followed the parameterizations given by Fernández et al. (1994) for the particle model and Zhang and Ghoniem (1994) for the plume rise calculations.

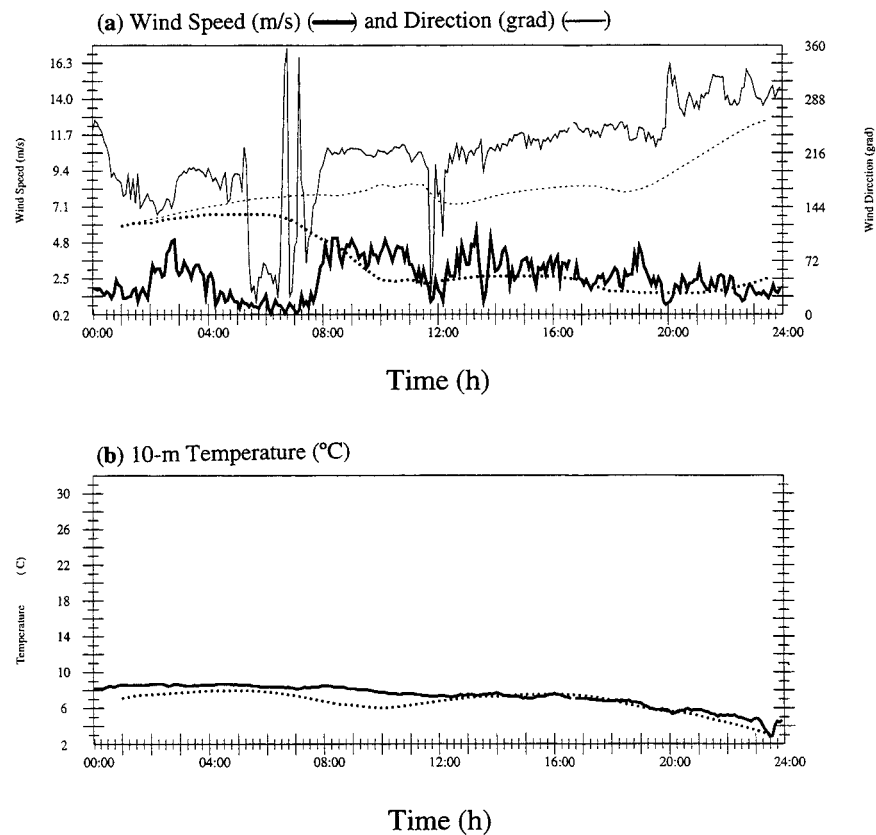


FIG. 10. Same as Fig. 9 but for 14 December 1996.

Figures 14a,b show the predicted  $\text{SO}_2$  ground-level concentration obtained for two different days in July and December, sunny and cloudy, respectively, in comparison with measurements (continuous line) obtained at GLC stations located within the area of simulation in the direction of the plume [F-7, F-6, and F-4 (see Fig. 1)]. Different sets of time series  $\xi(t)$  were used for comparison. The original values of  $\xi(t)$  were modified in two ways: 1) by adding zero mean Gaussian noise and dispersion  $\epsilon$  or 2) by adding a constant value.

In the first case (see the dashed lines around the solid one), the main GLC peaks were approximately reproduced for both days independent of the value of  $\epsilon$  [ $\epsilon \in (0, 0.2)$ ]. However, when a constant value of 0.2 was added, the maximum of concentration was much lower. Here, the mixed-layer depth  $z_i$  is lower for higher values of cloud absorption, which favor a decrease of GLC because the particles are not trapped by this convective structure that develops during the day.

When no cloud absorption was considered in modeling the heat budget,  $\xi = 0$  in Eqs. (11)–(21), the amount of predicted GLC was much higher than the measured values. We also used a set of forecast cloud absorption values provided by the Spanish National Weather Service, each 6 h, but it was not very successful because the resolution was poor for the relatively small area, and they did not account for the 24-h periodicity

that is an essential part of the cloud cover and the boundary layer dynamics.

#### 4. Summary and conclusions

A nonlinear forecasting method has been applied successfully to the prediction of cloud absorption 24 h in advance. The method is based on the reconstruction of a chaotic strange attractor and the construction of a predictor map using Farmer and Siderowich's (1987) and Casdagli's methods (1989) with piecewise functions for a time series of cloud absorption percentages obtained from the Meteosat. The results were used by a hydrostatic meteorological model for daily prediction of a plume transport from a power plant. Prediction of plume transport combines the meso- $\beta$  meteorological model and a nonreactive Lagrangian adaptive plume model (Ludwig et al. 1989) to obtain a complete air pollution forecast for 12–36 h in advance. The prediction model uses meso- $\alpha$  numerical predictions from the Spanish weather service for boundary conditions. Predictions can be obtained in approximately 3 h on a medium-sized workstation.

Our cloud absorption time series has passed a number of tests for a low-dimensional chaotic attractor that confirm that the presence of noise; although noise exists, it does not overwhelm the intrinsic nature of its deter-

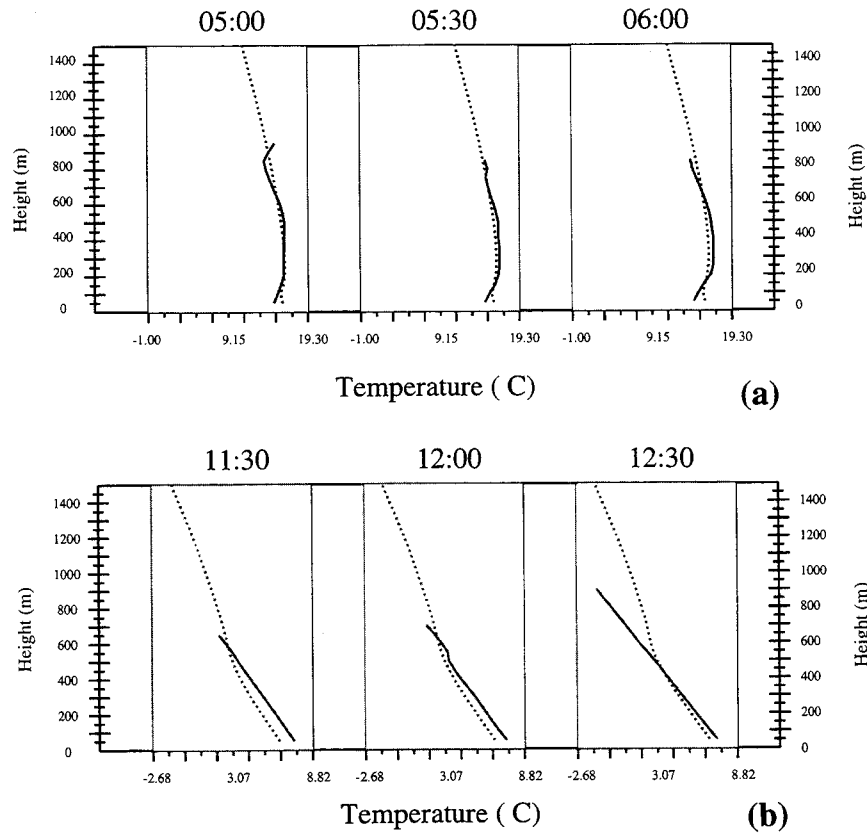


FIG. 11. Predicted (dots) and sodar-measured (line) temperature profiles for (a) 14 July and (b) 14 December 1996.

ministic dynamics. The results presented in this paper support this idea. Clearly, the low-frequency part of the power spectrum shown in Fig. 4 containing the daily 24-h period plays an important role in the low-dimensional, deterministic appearance of the dynamics. Nevertheless, as pointed out by Lorenz (Lorenz 1991), “the

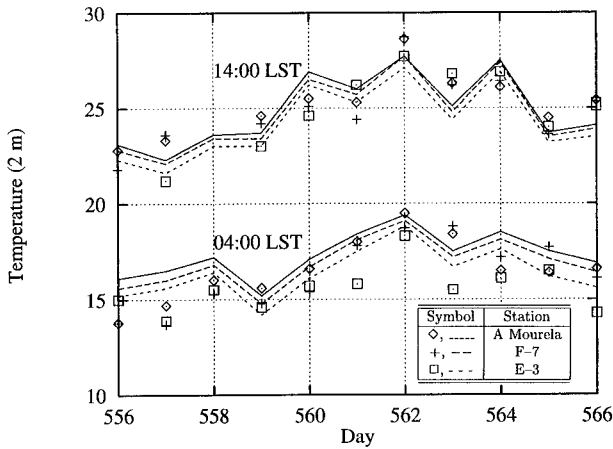


FIG. 12. Comparison of predicted and observed surface temperatures at three different meteorological stations: A Mourela, F-7, and E-3 for 0400 and 1400 LST.

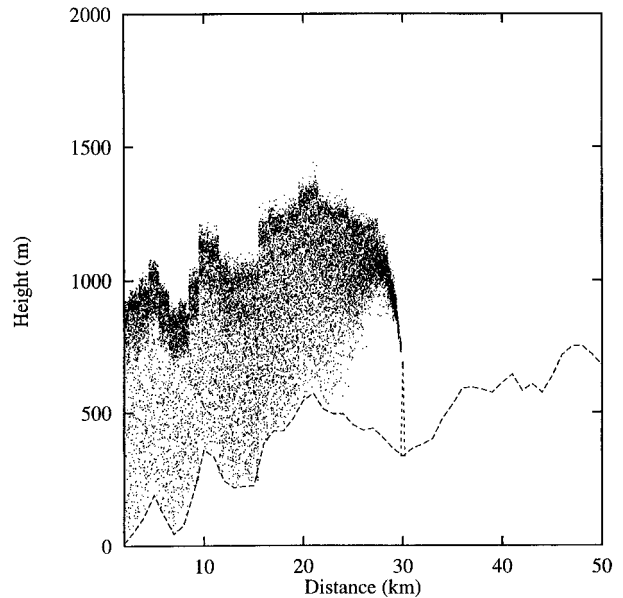


FIG. 13. Modeled vertical plume profile for 1700 LST 14 July 1996 projected onto a plane.

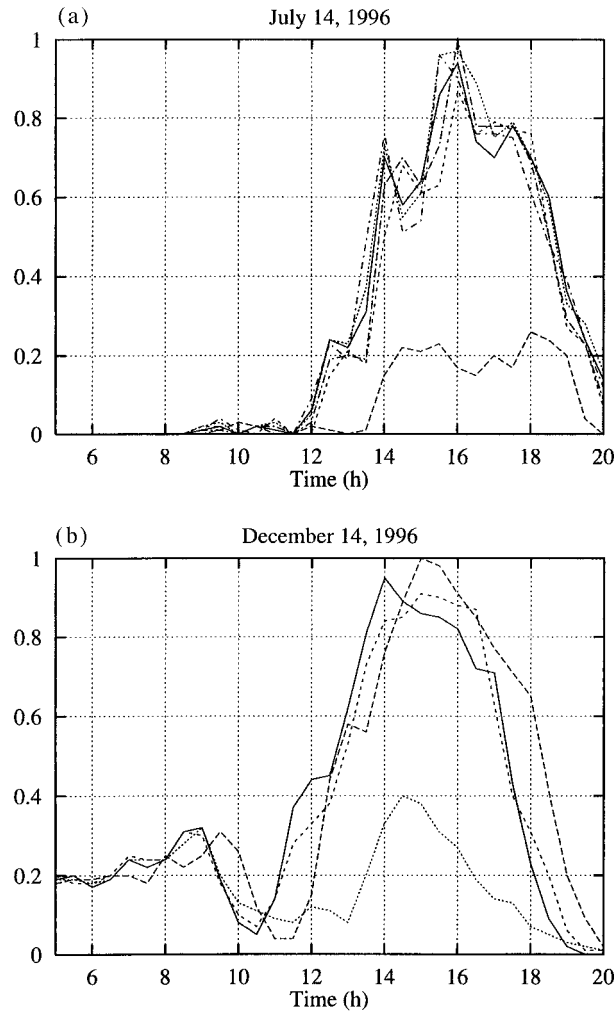


FIG. 14. Time evolution of ground-level  $\text{SO}_2$  concentration (GLC) measured (continuous line) and predicted (dashed lines) for (a) 14 July and (b) 14 December 1996.

atmosphere might be viewed as a loosely coupled set of lower dimensional subsystems,” we must correlate our cloud absorption time series with existing records of wind velocity, air pressure, humidity, etc., in north-western Spain where the measurements were taken, to identify the fundamental variables determining the dynamics and to find the other sources of determinism.

On the other hand, the nonlinear forecasting method presented here reveals the possibilities of short-term predictions of atmospheric parameters whose dynamics would make it very difficult to obtain a prognostic equation by other means.

Finally, we wish to emphasize that the whole system of forecasting models that we have described has been successful in forecasting the most important plume impacts around the As Pontes power plant. These models have been run routinely to provide forecasts under a large variety of conditions since 1995.

*Acknowledgments.* We wish to thank Tassos Bountis and his Group of Nonlinear Dynamics from Patras (Greece) for helpful discussions and suggestions. The computational time provided by the Centro de Supercomputación de Galicia (Spain) is gratefully acknowledged. This work is supported in part by Endesa.

#### APPENDIX A

##### Nonlinear Tools for Chaotic Time Series Analysis

The reconstructed phase space given by Eq. (23) is used to forecast the solution of Eq. (22) for a given point in the strange attractor  $\Xi$ , during a period of time  $T$ .

In principle  $\tau$  is arbitrary as long as the values of  $\xi_n$  and  $\xi_{n+\tau}$  in Eq. (23) are not highly correlated. If  $\tau$  is too small, the coordinates become singular so that  $\xi_n \approx \xi_{n+\tau}$ . If  $\tau$  is too big, chaos makes  $\xi_n$  and  $\xi_{n+\tau}$  causally disconnected by amplification of noise. In practice,  $\tau$  is chosen by trial and error, searching for optimal results. Other methods for estimating  $\tau$  have been suggested by Fraser and Swinney (1986); they require that the mutual information and its first minimum be determined. When the embedding dimension increases, the method requires the estimation of saturation values of the marginal redundancy, which is a means of how well a particular value in a sequence can be predicted from  $m$  of its predecessors; however, this method enhances the noise effects. Another recent method (Lai et al. 1996) proposes to estimate an upper bound for the proper time delay, but it is highly affected by noise. We should stress here that there is probably no unique optimal choice of delay, but a compromise to avoid choosing so small a time delay that the attractor collapses along the line  $\xi_n = \xi_{n+\tau} = \dots = \xi_{n+(m-1)\tau}$ , but not so large that the attractor tends to localize in only a small portion of the available space (Sauer et al. 1991).

Now, it is well known that Whitney’s embedding theorem (Whitney 1936; Hirsch 1976) guarantees that a  $d$ -dimensional manifold can be smoothly embedded in  $(2d + 1)$ -dimensional space (i.e., without crossing itself). Clearly, if the dimension  $d$  of the embedding space is too small, the orbit  $\Xi_n$  tends to completely fill the available  $d$ -dimensional space. On the other hand, if  $m$  increases beyond the embedding dimension  $m$ , some of the geometric properties of the dynamics are expected to remain unchanged for  $d \geq m$ .

One of such geometric property is the correlation dimension of our data  $\nu$ , which can be measured by the Grassberger–Procaccia method (Grassberger and Procaccia 1983) by means of the correlation integral  $C(r; m)$ , which is given by the relation

$$C(r; m) = \lim_{N \rightarrow \infty} \frac{1}{N^2} \sum_{i,j=1}^N \Theta[r - \|\Xi_j - \Xi_i\|], \quad (\text{A1})$$

where  $\Theta(\alpha)$  is the Heaviside function and  $\|\Xi_j - \Xi_i\|$  denotes the Euclidean norm for some  $r > 0$  between the states  $\Xi_j$  and  $\Xi_i$  in the  $m$ -dimensional reconstructed

space given by Eq. (23). The correlation integral  $C(r; m)$  is expected to scale as a power of the radius  $r$ ,

$$C(r; m) \propto r^{\nu(m)}, \quad \text{as } r \rightarrow 0. \quad (\text{A2})$$

The slope of the curve of  $\log[C(r; m)]$  versus  $\log(r)$ , that is,

$$\nu(m) = \lim_{r \rightarrow 0, m \rightarrow \infty} \frac{d\{\log[C(r; m)]\}}{d[\log(r)]}, \quad (\text{A3})$$

is called the correlation dimension. Now, if our data lie on an attractor and the dynamics is characterized by a deterministic chaos,  $\nu$  is expected to be a (close) lower bound of the fractal (Hausdorff) dimension  $D$  of the attractor, that is,  $\nu \leq D$  (Schuster 1988). From the previously mentioned Whitney's theorem, we can find a smooth embedding of the attractor as  $m = 2D + 1$ .

According to a formula proposed by Bountis et al. (1993), the number  $N$  of data points used in the calculations should satisfy

$$N \geq N_{\min}, \quad N_{\min} = 10^{2+0.4D}. \quad (\text{A4})$$

Other possible lower bounds for  $N$  are also described in Nerenberg and Essex (1990).

Finally, to complete the chaotic analysis of the experimental data the largest Lyapunov exponent must be calculated; that is, the largest rate of divergence of initially nearby trajectories under time evolution in an  $m$ -dimensional embedding space. We used the algorithm proposed by Wolf et al. (1985), although other methods can be found in the literature (Sano and Sawada 1985; Eckmann et al. 1986; Zeng et al. 1991). A positive Lyapunov exponent,  $\lambda$ , means that there exists a direction in the phase space along which the distance of two neighboring trajectories grows exponentially. In other words, there is at least one direction in phase space along which the orbits exhibit unstable (chaotic) behavior.

#### APPENDIX B

##### Notations

$U$	West–east wind component ( $\text{m s}^{-1}$ )
$V$	South–north wind component ( $\text{m s}^{-1}$ )
$W$	Vertical wind component ( $\text{m s}^{-1}$ )
$\theta$	Potential temperature (K)
$q_3$	Specific humidity ( $\text{kg kg}^{-1}$ )
$\pi$	Scaled pressure
$\psi$	Potential temperature lapse rate at $z_i$
$g$	Gravity acceleration ( $9.8 \text{ m s}^{-2}$ )
$S$	Effective solar constant
$A_S$	Absorption by atmospheric gases
$Z$	Solar zenith angle
$\alpha_S$	Albedo of ground surface
$\alpha_W$	Albedo of water surface
$Q_S$	Solar radiative flux
$Q_{LD}$	Downward longwave radiation
$Q_{LU}$	Upward longwave radiation
$Q_H$	Sensible heat flux from surface to atmosphere

$Q_E$	Latent heat flux
$Q_W$	Water surface radiation
$Q_A$	Atmospheric radiation over sea surface
$\rho_s$	Density of soil
$c_s$	Heat capacity of soil per unit mass
$k_s$	Thermal diffusivity of soil
$Y$	24 h
$T_M$	Deep soil temperature (K)
$\rho_w$	Density of water ( $1000 \text{ kg m}^{-3}$ )
$c_w$	Specific heat of water ( $4100 \text{ J kg}^{-1} \text{ K}^{-1}$ )
$L_v$	Latent heat of vaporization of water
$\gamma$	Bowen's constant ( $62.7 \text{ Pa K}^{-1}$ )
$\sigma$	Stefan–Boltzmann constant ( $5.67 \times 10^{-8} \text{ W m}^{-2} \text{ K}^{-4}$ )
$H$	Mean depth of the sea coast (m)
$R_h$	Relative humidity ( $0 \leq R_h \leq 1$ )

#### REFERENCES

- Abarbanel, H. D. I., 1996: *Analysis of Observed Chaotic Data*. Springer-Verlag, 288 pp.
- , R. Brown, and J. B. Katke, 1990: Prediction in chaotic nonlinear systems: Methods for time series with broadband Fourier spectra. *Phys. Rev.*, **41A**, 1782–1807.
- , —, J. J. Sidorowich, and L. Sh. Tsimring, 1993: The analysis of observed chaotic data in physical systems. *Rev. Mod. Phys.*, **65**, 1331–1392.
- Arking, A., 1964: Latitudinal distribution of cloud cover from *Tiros-III* photographs. *Science*, **143**, 569–572.
- Berkowicz, R., and L. P. Prahm, 1982: Evaluation of the profile method for estimation of surface fluxes of momentum and heat. *Atmos. Environ.*, **16**, 2809–2819.
- Blackadar, A. K., 1979: High-resolution models of the planetary boundary layer. *Adv. Environ. Sci. Eng.*, **1**, 50–85.
- Blanke, B., and P. Delecluse, 1993: Variability of the tropical Atlantic Ocean simulated by a general circulation model with two different mixed layer physics. *J. Phys. Oceanogr.*, **23**, 1363–1388.
- Bountis, T., L. Karakatsanis, G. Papaioannou, and G. Pavlos, 1993: Determinism and noise in surface temperature time series. *Ann. Geophys.*, **11**, 947–959.
- Businger, J. A., J. C. Wyngaard, T. Izumi, and E. F. Bradley, 1971: Flux–profile relationships in the atmospheric surface layer. *J. Atmos. Sci.*, **28**, 181–189.
- Casdagli, M., 1989: Nonlinear prediction of chaotic time series. *Physica D*, **35**, 335–356.
- Deardorff, J. W., 1974: Three-dimensional numerical study of the height and mean structure of a heated planetary boundary layer. *Bound.-Layer Meteor.*, **7**, 81–106.
- , 1978: Efficient prediction of ground surface temperature and moisture, with inclusion of a layer of vegetation. *J. Geophys. Res.*, **83**, 1889–1903.
- Eckmann, J. P., S. O. Kamphorst, D. Ruelle, and S. Ciliberto, 1986: Lyapunov exponents from time series. *Phys. Rev.*, **34A**, 4971–4979.
- Elgar, S., and G. Mayer-Kress, 1989: Observations of the fractal dimension of deep- and shallow-water ocean surface gravity waves. *Physica D*, **37**, 104–108.
- Enger, L., 1990: Simulation of dispersion in moderately complex terrain. Part A: The fluid dynamic model. *Atmos. Environ.*, **24A**, 2431–2446.
- , D. Koracin, and X. Yang, 1993: A numerical study of the boundary layer dynamics in a mountain valley. Part I: Model validation and sensitivity experiments. *Bound.-Layer Meteor.*, **66**, 357–394.
- Farmer, J. D., and G. G. Siderowich, 1987: Predicting chaotic time series. *Phys. Rev. Lett.*, **59**, 845–848.
- Fernández, J. F., L. Cremades, and J. M. Baldasano, 1994: Dispersion modelling of a tall stack plume in the Spanish Mediterranean coast by a particle model. *Atmos. Environ.*, **11**, 1331–1341.

- Fraedrich, K., 1986: Estimating the dimensions of weather and climate attractors. *J. Atmos. Sci.*, **43**, 419–432.
- Fraser, A. M., and H. L. Swinney, 1986: Independent coordinates for strange attractors from mutual information. *Phys. Rev.*, **33A**, 1134–1140.
- Grassberger, P., and I. Procaccia, 1983: Measuring the strangeness of strange attractors. *Physica D*, **9**, 189–208.
- Guckenheimer, G., and G. Buzyna, 1983: Dimension measurements for geostrophic turbulence. *Phys. Rev. Lett.*, **51**, 1438–1441.
- Haltiner, G. J., and R. T. Williams, 1980: *Numerical Prediction and Dynamic Meteorology*. John Wiley and Sons, 477 pp.
- Hirsch, M. W., 1976: *Differential Topology*. Springer-Verlag, 137 pp.
- Idso, S. B., and R. D. Jackson, 1969: Thermal radiation from the atmosphere. *J. Geophys. Res.*, **74**, 3397–3403.
- Isliker, H., and J. Kurths, 1993: A test for stationarity: Finding parts in time series APT for correlation dimension estimates. *Int. J. Bif. Chaos*, **3**, 1573–1579.
- Kondratyev, J., 1969: *Radiation in the Atmosphere*. Academic Press, 212 pp.
- Lai, Y.-C., D. Lerner, and R. Hayden, 1996: An upper bound for the proper delay time in chaotic time-series analysis. *Phys. Lett.*, **218A**, 30–34.
- Li, Z., H. W. Barker, and M. Moreau, 1995: The variable effects of clouds on atmospheric absorption of solar radiation. *Nature*, **376**, 486–490.
- Lorenz, E. N., 1991: Dimension of weather and climate attractors. *Nature*, **353**, 241–244.
- Ludwig, F. L., R. Salvador, and R. Bornstein, 1989: An adaptive volume plume model. *Atmos. Environ.*, **23**, 127–138.
- Malraison, B., P. Atten, P. Bergé, and M. Dubois, 1983: Dimension of strange attractors: An experimental determination for the chaotic regime of two convective systems. *J. Phys. Lett.*, **44L**, 897–902.
- Manuca, R., and R. Savit, 1996: Stationarity and nonstationarity in time series analysis. *Physica D*, **99**, 134–161.
- McCumber, M. C., and R. A. Pielke, 1991: Simulations of the effects of surface fluxes of heat and moisture in a mesoscale numerical model. Part I: Soil layer. *J. Geophys. Res.*, **86**, 9929–9938.
- Minnis, P., and E. F. Harrison, 1984: Diurnal variability of regional cloud and clear-sky radiative parameters derived from GOES data. Part I: Analysis method. *J. Climate Appl. Meteor.*, **23**, 993–1011.
- Nerenberg, M. A. H., and C. Essex, 1990: Correlation dimension and systematic geometric effects. *Phys. Rev.*, **42A**, 7065–7074.
- Nicolis, C., and G. Nicolis, 1984: Is there a climate attractor? *Nature*, **311**, 529–532.
- O'Brien, J. J., 1970: A note on the vertical structure of the eddy exchange coefficient in the planetary boundary layer. *J. Atmos. Sci.*, **27**, 1213–1215.
- Orlob, G. T., and N. Marjanovic, 1989: Heat exchange. *Mathematical Submodels in Water Quality Systems*, B. A. Schrefler and O. C. Zienkiewicz, Eds., Balkema, 303–310.
- Osborne, A. R., and A. Provenzale, 1989: Finite correlation dimension for stochastic systems with power-law spectra. *Physica D*, **35**, 357–381.
- Pavlos, G. P., L. Karakatsanis, J. B. Latoussakis, D. Dialeitis, and G. Papaioannou, 1994: Chaotic analysis of a time series composed of seismic events recorded in Japan. *Int. J. Bif. Chaos*, **4**, 87–98.
- Pérez-Muñuzuri, V., J. A. Souto, J. Ramírez, and J. J. Casares, 1995: Two point boundary problem for wind field forecasting. *Fluid Physics*, M. G. Velarde and C. I. Christov, Eds., World Scientific, 571–583.
- , M. J. Souto, J. J. Casares, and V. Pérez-Villar, 1996: Terrain-induced focusing of wind fields in the mesoscale. *Chaos, Solitons Fractals*, **7**, 1479–1494.
- Pielke, R. A., 1984: *Mesoscale Meteorological Modeling*. Academic Press, 612 pp.
- , and Y. Mahrer, 1975: Technique to represent the heated-planetary boundary layer in mesoscale models with coarse vertical resolution. *J. Atmos. Sci.*, **32**, 2288–2308.
- , and C. L. Martin, 1981: The derivation of a terrain-following coordinate system for use in a hydrostatic model. *J. Atmos. Sci.*, **38**, 1707–1713.
- Portela, L. I., and R. Neves, 1994: Modelling temperature distribution in the shallow Tejo estuary. *Advances in Water Resources Technology and Management*, G. Tsakiris and M. A. Santos, Eds., Balkema, 457–463.
- Prata, A. J., 1996: A new long-wave formula for estimating downward clear-sky radiation at the surface. *Quart. J. Roy. Meteor. Soc.*, **122**, 1127–1151.
- San José, R., 1991: A simple approach to evaluate mixed layer depths. *Environ. Software*, **6**, 161–167.
- Sano, M., and Y. Sawada, 1985: Measurement of the Lyapunov spectrum from a chaotic time series. *Phys. Rev. Lett.*, **55**, 1082–1085.
- Sauer, T., J. A. Yorke, and M. Casdagli, 1991: Embedology. *J. Stat. Phys.*, **65**, 579–616.
- Schuster, H. G., 1988: *Deterministic Chaos*. 2d ed. Physik Verlag, 345 pp.
- Short, D. A., and J. M. Wallace, 1980: Satellite-inferred morning-to-evening cloudiness changes. *Mon. Wea. Rev.*, **108**, 1160–1169.
- Smeda, M. S., 1979: Incorporation of planetary boundary-layer processes into numerical forecasting models. *Bound.-Layer Meteor.*, **16**, 115–129.
- Souto, J. A., V. Pérez-Muñuzuri, F. L. Ludwig, and J. J. Casares, 1994: Meteorological and atmospheric diffusion modeling for air pollution forecasting. *Computer Techniques in Environmental Studies V*, P. Zannetti, Ed., *Pollution Modeling*, Computational Mechanics, 281–288.
- , —, M. DeCastro, J. J. Casares, and J. Abadía, 1996: Application of short and 24 hours air pollution forecasting around a power plant. *Air Pollution IV*, B. Caussade, H. Power, and C. A. Brebbia, Eds., *Monitoring, Simulation and Control*, Computational Mechanics, 21–30.
- , —, —, M. J. Souto, J. J. Casares, and T. Lucas, 1998: Forecasting and diagnostic analysis of plume transport around a power plant. *J. Appl. Meteor.*, **37**, 1068–1083.
- Stauffer, D. R., N. L. Seaman, T. T. Warner, and A. M. Lario, 1993: Application of an atmospheric simulation model to diagnose air-pollution transport in the Grand Canyon region of Arizona. *Chem. Eng. Commun.*, **121**, 9–25.
- Stull, R. B., 1991: *An Introduction to Boundary Layer Meteorology*. Kluwer Academic, 666 pp.
- Sugihara, G., and R. M. May, 1990: Nonlinear forecasting as a way of distinguishing chaos from measurement error in time series. *Nature*, **344**, 734–741.
- Tag, P. M., F. W. Murray, and L. R. Koenig, 1979: A comparison of several forms of eddy viscosity parameterization in a two-dimensional cloud model. *J. Appl. Meteor.*, **18**, 1429–1441.
- Takens, F., 1981: Detecting strange attractors in turbulence. *Lecture Notes in Mathematics*, D. A. Rand and L. S. Young, Eds., Vol. 898, Springer, 366–381.
- Theiler, J., and S. Eubank, 1993: Don't blench chaotic data. *Chaos*, **3**, 771–783.
- Vonder Haar, T. H., and Coauthors, 1981: Measurements of the earth radiation budget from satellites during the first GARP Global Experiment. *Adv. Space Res.*, **1**, 285–297.
- Warner, T. T., and N. L. Seaman, 1990: A real-time, mesoscale numerical weather-prediction system used for research, teaching, and public service at The Pennsylvania State University. *Bull. Amer. Meteor. Soc.*, **71**, 792–805.
- Weygandt, S. S., and N. L. Seaman, 1994: Quantification of predictive skill for mesoscale and synoptic-scale meteorological features as a function of horizontal grid resolution. *Mon. Wea. Rev.*, **122**, 57–71.
- Whitney, H., 1936: Differentiable manifolds. *Ann. Math.*, **37**, 137–143.
- Wolf, A., J. B. Swift, H. L. Swinney, and J. Vastano, 1985: Determining Lyapunov exponents from a time series. *Physica D*, **16**, 285–317.
- Yamada, T., and G. Mellor, 1975: A simulation of the Wangara atmospheric boundary layer data. *J. Atmos. Sci.*, **32**, 2309–2329.
- Zeng, X., R. Eykholt, and R. A. Pielke, 1991: Estimating the Lyapunov-exponent spectrum from short time series of low precision. *Phys. Rev. Lett.*, **66**, 3229–3232.
- Zhang, X., and A. F. Ghoniem, 1994: A computational model for the rise and dispersion of wind-blown, buoyancy-driven plumes Part II: Linearly stratified atmosphere. *Atmos. Environ.*, **28**, 3005–3018.